Transition to fully developed turbulence in quasi-two-dimensional electromagnetic layers

Seunghwan Shin * and Filippo Coletti
Department of Mechanical and Process Engineering, ETH Zurich, 8092 Zurich, Switzerland

Nicholas Conlin
Department of Mechanical and Aerospace Engineering, Princeton University, Princeton, New Jersey 08544, USA

(Received 9 June 2023; accepted 28 August 2023; published 15 September 2023)

Forced two-dimensional turbulence lives on the balance between the energy input and two dissipative mechanisms, viscosity and linear friction, resulting in a double cascade of energy and enstrophy. While it is known that the energy cascade is governed by the Reynolds number $\mathrm{Re}_\alpha = u_{\mathrm{rms}}/(\alpha L_\mathrm{f})$, it has been more convenient to report $\mathrm{Re} = u_{\mathrm{rms}} L_\mathrm{f}/\nu$ (where u_{rms} is the fluctuating velocity, L_f the forcing scale, α the friction coefficient, and ν the kinematic viscosity). Therefore, it is unclear for which range of parameters the various hallmarks of fully developed turbulence will emerge. Here we use multiple laboratory setups in which a quasi-two-dimensional flow is generated in electromagnetic layers of fluids, over a wide range of Re and Re_α. The friction coefficient measured during turbulence decay is correctly estimated by a linear shear assumption, allowing us to readily estimate Re_α. We consider several observables characterizing the turbulence development: the fraction of energy input converted to fluctuating energy, the correlation scale of the flow, the velocity structure functions, the probability distribution of the velocity fluctuations and velocity differences, the single-particle diffusivity, and the separation time between particle pairs. All descriptors collapse on master curves against Re_α, providing a criterion for fully developed turbulence for this class of flows. Moreover, dedicated experiments in which the local Re and Re_α are spatially decoupled show that only the latter is correlated with the growth of turbulent energy. Finally, a scaling relation is proposed that relates the amount of energy going to the large scales to the forcing scale-to-layer thickness ratio.

DOI: 10.1103/PhysRevFluids.8.094601

I. INTRODUCTION

In the last decades, the interest in two-dimensional (2D) turbulence has grown far beyond scientific curiosity in fundamental dynamics, and it has been fueled by its relevance to geophysical flows in the atmosphere and the ocean [1–3]. Indeed, while strictly 2D turbulent flows are not physically realizable, they share basic similarities with high-aspect-ratio systems in which confinement in one direction inhibits vortex stretching. The resulting phenomenology famously differ from classic three-dimensional (3D) turbulence, notably in that a double cascade ensues, with energy flowing to the large scales and enstrophy flowing to the small ones (see [4–6]). These and other signature features of 2D turbulence have thus been investigated experimentally in quasi-two-dimensional (Q2D) laboratory apparatuses, especially in thin electromagnetic layers (EMLs) of conductive fluids and in gravity-driven soap films [6,7]. Recently, it has also been shown that 2D turbulence behavior

*seshin@ethz.ch

is exhibited by a liquid subject to Faraday waves induced by vertical oscillation of the container [8,9]. With the important constraint that the motion in the third direction be kept negligibly small [10,11], these setups allow investigating the Q2D flow by tracking suspended tracers both in the Eulerian frame [via particle image velocimetry (PIV)] and in the Lagrangian frame [via particle tracking velocimetry (PTV)]. An immediate experimental advantage is that, unlike in 3D flows, the fluid motion can be fully captured by planar imaging, without the complexities and costs associated with volumetric velocimetry [12]. We stress that the EML system can never be fully 2D, in particular due to the no-slip boundary condition at the bottom surface. However, multiple recent studies have demonstrated that the Q2D flow assumption is reasonably well approximated in such systems. Tithof *et al.* [11] evaluated out-of-plane motions and vertical velocity profiles for various flow configurations, and found that the Q2D assumption was tenable in particular for the single-layer and immiscible double-layer configurations. Moreover, Martell *et al.* [13] measured the misalignment between the velocity vectors from tracers in between and above both layers of an immiscible double-layer system, and found that the local alignment was satisfied within 6% even for a relatively thick 6-mm layer.

While the early and seminal contributions on 2D turbulence were concerned with the flow evolution during its natural decay [14], recent studies have more often focused on steady-state systems. Those are usually modeled via a large-scale friction that balances the external forcing, for which the governing 2D Navier-Stokes equation reads

$$\partial_t \boldsymbol{u} + \boldsymbol{u} \cdot \nabla \boldsymbol{u} = -\frac{1}{\rho}\nabla P + \nu \nabla^2 \boldsymbol{u} - \alpha \boldsymbol{u} + \boldsymbol{f}. \tag{1}$$

Here $\boldsymbol{u}$ and P are the velocity and pressure fields, ν is the kinematic viscosity, α is a coefficient of linear frictional damping (also known as Rayleigh friction) that arises due to the viscous dissipation along the depth of the fluid as a result of the no-slip boundary condition at the bottom solid boundary, and $\boldsymbol{f}$ is the forcing term acting at a scale L_f. This form underlines a further important difference with respect to 3D turbulence, i.e., the role of dissipation at the boundaries [6,15]: the input energy rate ϵ_I from the forcing is balanced not solely by the viscous dissipation ϵ_ν, but also by the frictional dissipation ϵ_α, $\epsilon_\mathrm{I} = \epsilon_\nu + \epsilon_\alpha$. While ϵ_ν acts predominantly at the Kolmogorov scale $L_\nu \equiv (\epsilon_\nu/\eta_\nu)^{1/2}$ (where η_ν is the viscous enstrophy dissipation), ϵ_α is associated with the scale $L_\alpha \equiv (\epsilon_\alpha/\eta_\alpha)^{1/2}$ (where η_α is the frictional enstrophy dissipation). The latter is related to the characteristic root-mean-square velocity, $L_\alpha \sim u_\mathrm{rms}/\alpha$, and provides a large-scale cutoff to the inverse cascade of energy. This duality implies the need for defining two Reynolds numbers. On the one hand, $\mathrm{Re} \equiv u_\mathrm{rms} L_\mathrm{f}/\nu$ quantifies the extent of the range $L_\nu \ll L \ll L_\mathrm{f}$, where the direct cascade of enstrophy takes place [6]: $\mathrm{Re} \sim (L_\mathrm{f}/L_\nu)^2$. On the other hand, the outer-scale Reynolds number $\mathrm{Re}_\alpha \equiv u_\mathrm{rms}/(\alpha L_\mathrm{f})$ quantifies the extent of the range $L_\mathrm{f} \ll L \ll L_\alpha$, associated with the inverse cascade of energy: $\mathrm{Re}_\alpha \sim L_\alpha/L_\mathrm{f}$. This association of the Reynolds number to the ratio of scales bounding the inertial range is common to various types of turbulence; e.g., it is analogous to what was recently proposed in [16] for 3D turbulence in which vortex stretching was artificially removed. We also remark that, alternatively to (1), several numerical studies utilize hypofriction, which concentrates the frictional dissipation at large scales. Such strategy can influence the extent of the inertial range over which the inverse energy cascade is observed [17].

Beyond these definitions, it is not straightforward to determine which parameter governs which process: while Re_α is directly related to the energy cascade range, it is the limit $\mathrm{Re} \to \infty$ that warrants $\epsilon_\nu/\epsilon_\alpha \to 0$, which in turn guarantees that all energy flows to the large scales [6]. As such, there are no established criteria to determine the portion of the input energy that is dissipated by frictional dissipation versus viscous dissipation. In general, it is acknowledged that Re_α is the main parameter to characterize the inverse cascade range. Still, in the literature Re is by far the most (and often the only) reported nondimensional parameter. With no ambition of being exhaustive, Table I lists the wide range of Re in several past experiments investigating 2D turbulence in EML systems

TABLE I. The ranges of Re in several previous studies exploring 2D turbulence in EML systems. SL, MDL, and IDL stand for a single fluid layer, two miscible layers, and two immiscible layers, respectively.

Reference	Fluid configuration	L_f (mm)	Re
[18]	SL	8	600–2400
[19]	MDL	15	100
[20]	MDL	50	500
[21]	SL	50	1500–2750
[22]	IDL	18	500
[31]	IDL	9	11–80
[23]	SL	25.4	185
[24]	MDL	25.4	300
[25]	MDL	25.4	200
[11]	MDL	25.4	50–740
Present paper	SL, IDL	19; 35	39–2025

(as we do in the present paper). The practice of using Re to describe the strength of the forcing is partly rooted in analogy with 3D turbulence (where there is little doubt that Re characterizes the transition to and the intensity of turbulence), and partly in the immediate availability of the fluid viscosity compared to the geometry-dependent friction coefficient. However, there is no agreement on the Re value (or range of values) for which 2D turbulence emerges and/or reaches a fully developed state. In part, this is due to the inherent challenge of defining such a multifaceted phenomenon as turbulence [26]. One may identify its onset with the development of space-time disorder [27], but even far beyond this point Q2D flows often maintain the fingerprint of the forcing structure, e.g., the array of magnets in EML systems. Indeed, flows in this regime, usually observed for $\mathrm{Re} < 200$, are rather qualified as "nonperiodic," "chaotic," or "weakly turbulent" [28–30]. Xia *et al.* [31] summed up the state of the matter, affirming that "there is no well accepted parameter to quantify the degree of turbulence development in 2D, and it is not clear whether the Reynolds number [Re] is a meaningful measure of it." They considered a wide range of laboratory Q2D flows (EML and Faraday-wave systems) in the range $\mathrm{Re} = 11$–188, and proposed that 2D turbulence development be quantified by a Lagrangian dispersion parameter; this appeared to reach the critical value for $\mathrm{Re} > 60$. Tithof *et al.* [11] considered multiple EML arrangements (a single fluid layer, two miscible layers, and two immiscible layers) and reported nonperiodic flow for $\mathrm{Re} > 200$; yet, the emergence of a broad range of scales became apparent only for $\mathrm{Re} > 500$. On the other hand, it has been hypothesized that friction may play a more central role than viscous dissipation. Sommeria [32] and Michel *et al.* [33] studied Q2D flows over a very wide range of *Rh*, a friction Reynolds number equivalent to Re_α, using single layers of liquid metals. In both studies *Rh* was taken as the dominant control parameter based on order-of-magnitude considerations. However, the effect of Re was not investigated, and the fluid layer thickness was such that significant 3D effects could not be excluded.

In the present paper, we use two EML apparatuses and different fluid layer configurations to visit a wide range of Re and Re_α, from the regular or periodic regime to fully developed turbulence. We use PIV and PTV to measure the flow in the Eulerian and Lagrangian frames, quantifying observables classically used to characterize hallmark features of turbulence. The objective is to determine whether, in such systems, the emergence and development of the various aspects of 2D turbulence are consistently associated with a specific range of Re or Re_α. The paper is organized as follows: in Sec. II we present the experimental setup and the imaging methodology; in Sec. III we report the results in terms of Eulerian and Lagrangian quantities; in Sec. IV we discuss the results and draw the main conclusions.

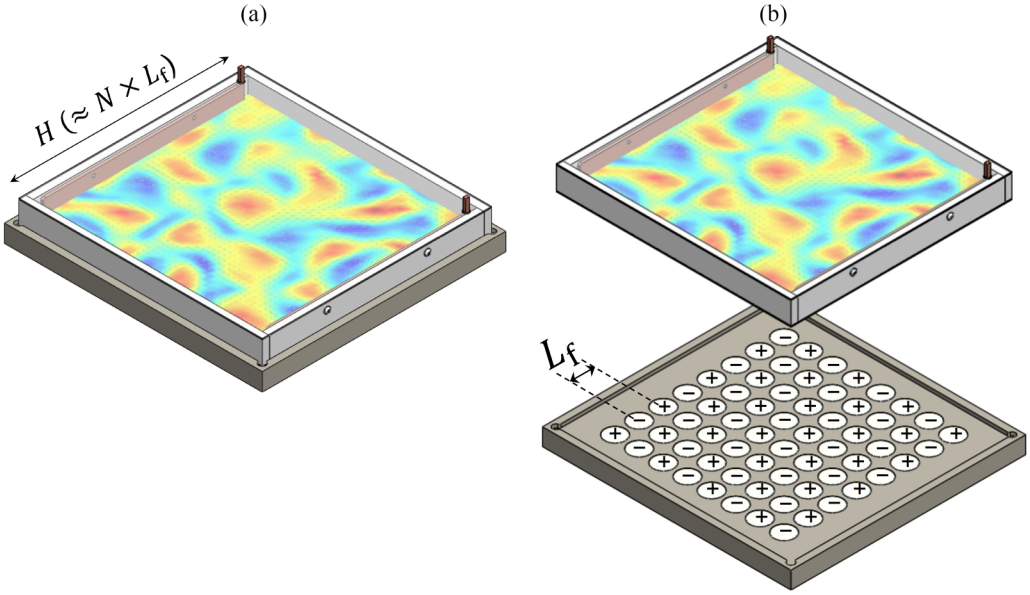

FIG. 1. (a) A schematic of our experimental apparatus. Its lateral dimension $H = 200$ mm for a smaller device and 300 mm for a larger device, and $H = N \times L_\mathrm{f}$, where N is the number of magnet spacings between the copper electrodes and L_f is the distance between the neighboring magnet centers. $N = 10$ for a smaller device and $N = 8$ for a larger device. $L_\mathrm{f} = 19$ mm for a smaller device and 35 mm for a larger device. Note that $H \approx N \times L_\mathrm{f}$. (b) Underneath the flow tray, $N \times N$ magnets separated by L_f on centers are installed in a checkerboard array with alternating direction of polarity.

II. EXPERIMENTAL METHODS

We utilize an EML system with magnets of alternating polarity in a checkerboard pattern as described in Fig. 1. We employ two similar setups of different dimensions. The first device features a tray of 200×200 mm^2 lying above a square array of 10×10 cylindrical neodymium-iron-boron (NdFeB) grade N52 magnets. The magnets are 12.7 mm in diameter and 3.18 mm in thickness, the magnetic field near their surface is 0.21 T, and their centers are separated by $L_\mathrm{f} = 19$ mm. The second device consists of a 320×320 mm^2 tray above an 8×8 array of N52 magnets. These are 30 mm in diameter and 10 mm in thickness, the magnetic field near their surface is 0.26 T, and they are spaced by $L_\mathrm{f} = 35$ mm. In both devices, copper electrodes are installed at opposite sides of the tray to apply dc current through a conductive fluid layer, introducing the Lorentz force driving the flow. During each experiment, we measure a temperature increase due to Joule heating smaller than 1 K, thus the variation in the fluid kinematic viscosity is negligible.

Using both setups, we combine single- and double-layer arrangements and different fluid layer thicknesses, realizing five different configurations to visit ranges of Re and Re_α, as listed in Table II. As a conductive fluid (subscript "c"), we use a 10% $CuSO_4$ aqueous solution (by mass) with a density $\rho_\mathrm{c} = 1080\,\mathrm{kg/m^3}$ and a kinematic viscosity indistinguishable from pure water, $\nu_\mathrm{c} = 1$ mm^2/s. In the immiscible double-layer configurations, FC-770 (3M) is used for the nonconductive layer fluid (subscript "NC"). Its density ($\rho_\mathrm{NC} = 1790\,\mathrm{kg/m^3}$) is higher compared to the conductive fluid, while the kinematic viscosity ($\nu_\mathrm{NC} = 0.79$ mm^2/s) is smaller. Therefore, it serves as a lubricating bottom layer, reducing the friction experienced by the driven fluid and allowing for higher Re_α compared to the single-layer counterpart at comparable Re. Indeed, assuming for simplicity a linear shear, the friction coefficient can be estimated as $\alpha = \pi^2 \nu_\mathrm{c}/(2h^2)$ for the single-layer setup and $\alpha = (\rho_\mathrm{NC}/\rho_\mathrm{c})[\nu_\mathrm{NC}/(h_\mathrm{c} h_\mathrm{NC})]$ for the double-layer setup, where h is the fluid layer thickness [6]. The accuracy of this relation in the considered EML systems will be verified in the next section.

TABLE II. List of the reported experiments.

Configuration	Description	Fluid(s)	α (s^{-1})	Re	Re_α
SL1 (■)	$h = 5$ mm, $L_f = 19$ mm	$CuSO_{4\,(aq)}$	0.1974	39–371	0.54–5.21
SL2 (●)	$h = 5$ mm, $L_f = 35$ mm	$CuSO_{4\,(aq)}$	0.1640	156–2025	0.78–10.08
SL3 (♦)	$h = 10$ mm, $L_f = 35$ mm	$CuSO_{4\,(aq)}$	0.0410	127–1573	2.53–31.36
IDL1 (▲)	$h = 5 + 5$ mm, $L_f = 35$ mm	FC-770, $CuSO_{4\,(aq)}$	0.0524	157–858	2.45–13.37
IDL2 (★)	$h = 5 + 3$ mm, $L_f = 35$ mm	FC-770, $CuSO_{4\,(aq)}$	0.0874	207–1609	1.93–15.02

The fluid is seeded by green fluorescent tracers, illuminated by a blue LED, and imaged by a FLIR Grasshopper3 camera. To prevent the particles from depositing and sticking on the bottom tray, in the single-layer configuration we use microspheres with density $\rho_p = 1000\,kg/m^3$ (Cospheric UVPMS-BG-1.00), so that $\rho_p < \rho_c$. In the double-layer configuration we have $\rho_p = 1100\,kg/m^3$ (Cospheric UVPMS-BG1.10), so that $\rho_c < \rho_p < \rho_{NC}$ and the tracers stay at the interface between both fluids. The particle diameter d_p ranges from 75 to 90 μm, ensuring faithful tracing of the flow. The field of view (FOV) is $140 \times 140\ mm^2$ (800×800 pixels) for the smaller device, and $245 \times 245\ mm^2$ (1024×1024 pixels) for the larger one. Both FOVs span the central part excluding the peripheral magnets, thus imaging a region where boundary effects are small. Images are acquired at frequencies ranging between 20 and 62.5 Hz depending on the setup and flow regime, typically ensuring a particle displacement around 5 pixels. For each investigated case, we typically track about 5000 particles per frame during a recording time of 100 s.

Eulerian velocity fields are obtained by PIV using an open-source software (PIVlab, [34]) with a final interrogation window of 16 pixels. Lagrangian trajectories are obtained with a standard PTV algorithm based on Crocker and Grier [35]. In each run, the PIV and PTV data are derived from the same image sequence. While it is generally more natural to extract Eulerian quantities from the former and Lagrangian ones from the latter, all the observables we present can be calculated from either data set and are found to agree well with each other (see Appendix A). To assess the degree to which the 2D flow condition is approximated, we quantify the out-of-plane motion by calculating the normalized divergence from the Eulerian fields [10,11] and find it to be typically smaller than 0.05.

The measurements quantitatively confirm the theoretical relations between the forcing parameters and the Reynolds number Re. This is measured by calculating

$$u_{rms} = \langle \boldsymbol{u}(\boldsymbol{x}, t) \cdot \boldsymbol{u}(\boldsymbol{x}, t) \rangle_{\boldsymbol{x},t}^{1/2}, \tag{2}$$

where the subscripts to the angle brackets denote averaging in both space $\boldsymbol{x}$ and time t. Definition of the Lorentz force (3) and dimensional arguments (4) [36,37] predict $Re \sim J^{1/2}$, where J is the current density:

$$f_b = \frac{|\mathbf{J} \times \mathbf{B}|}{\rho} = \frac{\frac{I}{Hh}\overline{B}}{\rho} = \frac{\frac{I}{V/H}\overline{B}}{\rho} = \frac{\frac{I}{V/(NL_f)}\overline{B}}{\rho} = \frac{NL_f I\overline{B}}{\rho V}, \tag{3}$$

$$f_b \sim \frac{u_{rms}^2}{L_f}, \tag{4}$$

$$Re = \frac{u_{rms} L_f}{\nu} \approx \left[\frac{L_f^2}{\nu} \left(\frac{N\overline{B}}{\rho L_f} \right)^{1/2} \right] J^{1/2}, \tag{5}$$

where f_b is the Lorentz force per unit mass, I is the applied dc current, H is the lateral size of the tray, $\overline{B}$ is the magnetic field strength (the overbar indicating depth average), N is the number of magnets spaced between both electrodes, and V is the test fluid volume. Figure 2(a) shows that not only the scaling relations but also the estimated prefactor in (5) apply well to our experiments. For

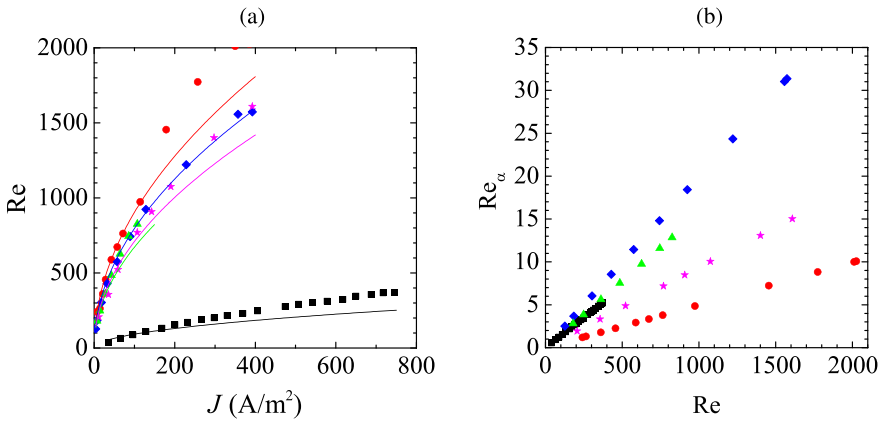

FIG. 2. (a) Re determined from root-mean-squared velocity as a function of current density J. Lines indicate predictions by (5). (b) Range of Re and Re$_\alpha$ in this paper. We study 58 cases from five different configurations. See Table II for explanation of the symbols.

consistency, the same symbols and color codes listed in Table II are used to make a comparison among results from different configurations.

Both Reynolds numbers can be written explicitly as a function of the forcing parameters:

$$\mathrm{Re} = \frac{L_\mathrm{f}^{3/2}\chi^{1/2}}{\nu}, \tag{6}$$

$$\mathrm{Re}_\alpha = \frac{\chi^{1/2}}{L_\mathrm{f}^{1/2}\alpha}, \tag{7}$$

where $\chi = N\overline{B}J/\rho$ (with units of acceleration) is proportional to the forcing amplitude, as defined for example in [38].

Figure 2(b) displays the 58 investigated cases in the Re-Re$_\alpha$ plane. Since the frictional damping is geometry dependent, so is the ratio between viscous and frictional Reynolds numbers: $\mathrm{Re}_\alpha/\mathrm{Re} = (2/\pi^2)(h/L_\mathrm{f})^2$ in the single-layer configuration, and $\mathrm{Re}_\alpha/\mathrm{Re} = (\rho_\mathrm{c}/\rho_\mathrm{NC})(\nu_\mathrm{c}/\nu_\mathrm{NC})(h_\mathrm{c}h_\mathrm{NC}/L_\mathrm{f}^2)$ in the double-layer configuration. Accordingly, using the different setups we can effectively decouple Re$_\alpha$ and Re, which allows us to evaluate their respective effects on the flow behavior.

III. RESULTS

This linear-shear assumption is possibly simplistic in 2D turbulence. Thus, we conduct spin-down experiments in both the single-layer and the double-layer configurations to determine whether Re$_\alpha$ based on this scenario agrees with the measured value. Following Fang and Ouellette [25], we realize steady-state flows at varying Reynolds numbers and remove forcing afterward by turning off the applied current to measure decay of the flows as a function of time. Fang and Ouellette [25] demonstrated multiple (exponentially) decaying stages in 2D turbulent flows, and also suggested that the second decay stage be interpreted as a regime of pure 2D turbulence, where energy is transported from smaller to larger scales and eventually damped by the large-scale frictional dissipation. Figure 3(a) displays our flow decays over three stages. We fit the data in the second regime to $\langle E_k(t)\rangle/\langle E_k(0)\rangle = \langle u^2(t)\rangle/\langle u^2(0)\rangle \sim \exp(-2\alpha t)$, to extract α and Re$_\alpha$. Figure 3(b) shows Re$_\alpha$ estimated based on the theory of linear shear (Re$_{\alpha,\mathrm{theory}}$) and the experimentally determined Re$_\alpha$ are indeed in reasonable agreement, with errors mostly lying within 15%. While small bias errors can occur for the different flow configurations, in Appendix B it is shown that using the measured

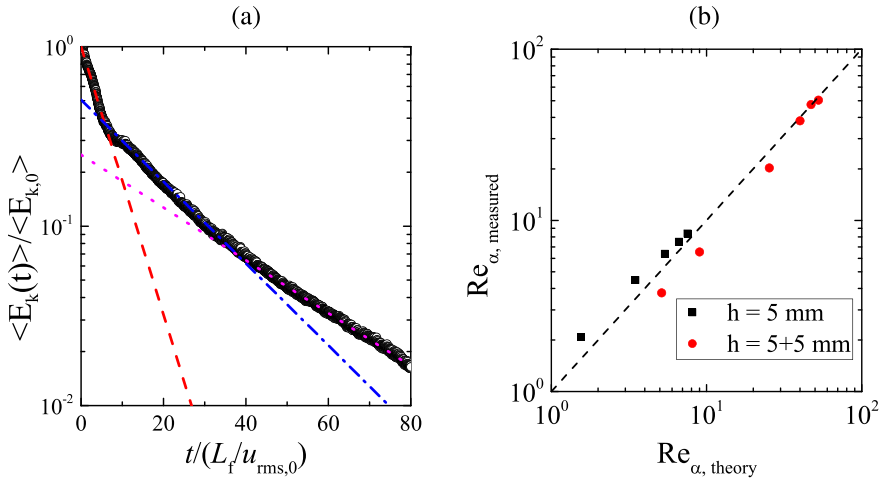

FIG. 3. (a) An example of spin-down experiment. The decaying kinetic energy is normalized by its steady-state value averaged over 10 s, and the time is normalized by $L_f/u_{rms,0}$, the characteristic eddy turnover time of the forcing. The red dashed, blue dash-dotted, and magenta dotted lines are exponential fits of three decaying regimes, with corresponding $\alpha = [11.6(L_f/u_{rms,0})]^{-1}$, $[38.1(L_f/u_{rms,0})]^{-1}$, and $[59.1(L_f/u_{rms,0})]^{-1}$, respectively. The second decay regime (blue dash-dotted) is taken to calculate α that gives $Re_{\alpha,measurement} = u_{rms,0}/(\alpha L_f) = 38.1$. (b) Comparison between Re_α based on a linear friction damping ($Re_{\alpha,theory}$) and from the spin-down experiments ($Re_{\alpha,measured}$). A black dashed line indicates equivalence.

friction coefficient versus the theoretical estimate leads to the same quantitative results. Therefore, we simply present $Re_{\alpha,theory}$ as Re_α in Table II and below.

A. Eulerian properties

We first consider the visual evidence of the transition to turbulence. In each considered configuration, a steady checkerboard array of counter-rotating vortices is observed at low forcing, giving way to an irregular flow field as Re is increased, as expected. This is illustrated in Figs. 4(a)–4(d) for the SL2 configuration. However, the transition happens at different Re for different configurations. Figures 4(e)–4(g) display instantaneous fields of velocity $\boldsymbol{u}$ and vorticity ($\boldsymbol{\omega} = \nabla \times \boldsymbol{u}$) of three different configurations, with similar $Re \approx 245$ and increasing Re_α. SL2 [Fig. 4(e)] displays a regular vortex array, although Re is well beyond the range in which several previous studies reported chaotic or even fully developed turbulence [29–31]; SL1 and IDL1 show a chaotic vortical structure. Temporal sequences (not shown) confirm that, at this Re, SL2 is at steady state while the other configurations evolve in time, with larger temporal fluctuations for larger Re_α.

These considerations are made quantitative by characterizing the temporal fluctuations of the velocity field. Applying Reynolds decomposition, we define

$$\langle E_{\text{total}} \rangle = \langle \boldsymbol{u}^2(\boldsymbol{x}, t) \rangle_{\boldsymbol{x},t}, \tag{8}$$

$$\langle E_{\text{mean}} \rangle = \langle \langle \boldsymbol{u}(\boldsymbol{x}, t) \rangle_t^2 \rangle_{\boldsymbol{x}}, \tag{9}$$

$$\boldsymbol{u}_{\text{fluc}}(\boldsymbol{x}, t) = \boldsymbol{u}(\boldsymbol{x}, t) - \langle \boldsymbol{u}(\boldsymbol{x}, t) \rangle_t, \tag{10}$$

$$\langle E_{\text{fluc}} \rangle = \langle \boldsymbol{u}_{\text{fluc}}^2(\boldsymbol{x}, t) \rangle_{\boldsymbol{x},t}. \tag{11}$$

Following Liao *et al.* [39], we investigate the partition of the total energy in mean and fluctuating energy, $\langle E_{\text{total}} \rangle = \langle E_{\text{mean}} \rangle + \langle E_{\text{fluc}} \rangle$. Figure 5 quantifies the fraction of the input energy that is

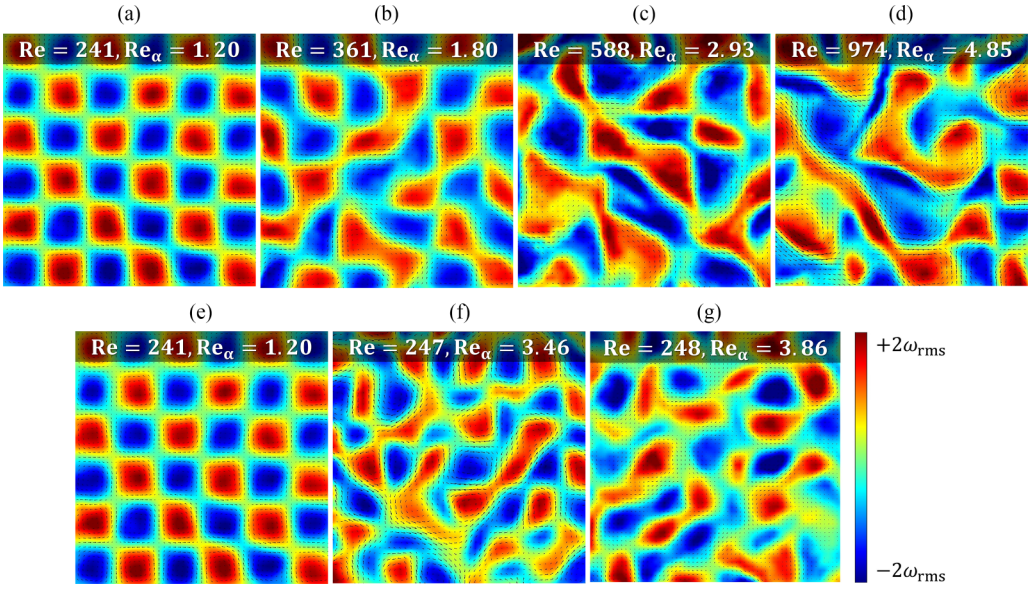

FIG. 4. Eulerian velocity fields and normalized vorticity maps from SL2 experiment at different Reynolds numbers, at (a) Re = 241, (b) Re = 361, (c) Re = 588, and (d) Re = 974. In each case, the colormap indicates $[-2\omega_{\rm rms}\ 2\omega_{\rm rms}]$, from blue to red. Instantaneous Eulerian velocity fields and normalized vorticity maps with Re ≈ 245 and increasing Re$_\alpha$ from three different configurations, (e) SL2, Re = 241, Re$_\alpha$ = 1.20, (f) SL1, Re = 247, Re$_\alpha$ = 3.46, and (g) IDL1, Re = 248, Re$_\alpha$ = 3.86.

transformed into temporal fluctuations, $\langle E_{\rm fluc}\rangle/\langle E_{\rm total}\rangle$, plotted as a function of both Re and Re$_\alpha$. The ratio grows for increasing Reynolds number, as expected. It appears to plateau above approximately 0.8, although we cannot conclusively determine whether an asymptote has been reached. Clearly, while the range of Re for which the plateau is reached is wide (Re ≈ 300–600), the curve collapse is much better as a function of Re$_\alpha$. Here and in the following, an exponential best fit to the latter is shown as a solid black curve (reported in Appendix A). A friction Reynolds number larger than Re$_\alpha$ ≈ 5 appears necessary to reach the fully developed state, i.e., a state such that further increase in

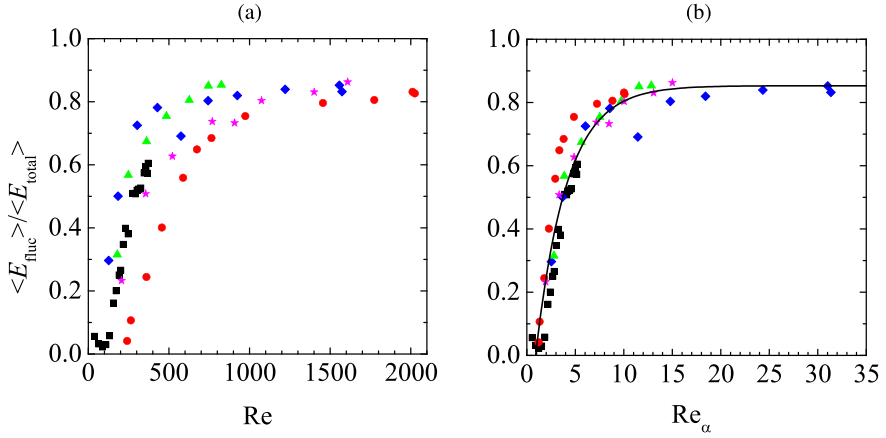

FIG. 5. Turbulence intensity defined as the normalized temporal fluctuation of the velocity, as a function of (a) Re and (b) Re$_\alpha$. A black solid line indicates an exponential best fit. See Table II for explanation of the symbols.

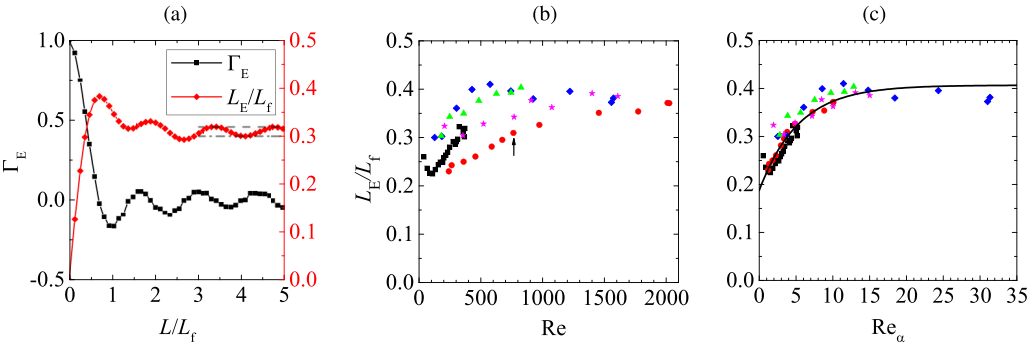

FIG. 6. An example of the Eulerian VACF (black) and the Eulerian length scale (L_E, red) at Re = 763 and $Re_\alpha = 3.80$. The mean of the furthest maximum (dashed) and minimum (dash-dotted) of oscillation is taken as L_E. (b) The normalized Eulerian length scales as a function of Re. The example of (a) is indicated with an arrow. (c) The same quantity as a function of Re_α. A solid black curve indicates an exponential best fit. See Table II for explanation of the symbols.

Re_α does not cause major changes in the observable, and an asymptotic behavior is reached around $Re_\alpha \approx 10$. We will see how this approximate level holds also for the development of other signature features of 2D turbulence.

With the flow becoming turbulent, the scales over which the velocity is spatially correlated also evolve. We define the Eulerian integral scale L_E using the velocity autocorrelation function (VACF) between two points $\boldsymbol{x}_0$ and $\boldsymbol{x}_0 + \boldsymbol{L}$, separated by a distance $|\boldsymbol{L}| = L$:

$$\Gamma_E(L) = \frac{\langle \boldsymbol{u}(\boldsymbol{x}_0, t) \cdot \boldsymbol{u}(\boldsymbol{x}_0 + \boldsymbol{L}, t) \rangle_{\boldsymbol{x}_0, \boldsymbol{L}, t}}{\langle \boldsymbol{u}(\boldsymbol{x}_0, t) \cdot \boldsymbol{u}(\boldsymbol{x}_0, t) \rangle_{\boldsymbol{x}_0, t}}. \tag{12}$$

It is conventional to define $L_E = \int_0^\infty \Gamma_E(L) dL$, with the integration extending in practice to separations beyond which the integral varies marginally. In the present case, the regularly alternating vortices are reflected in oscillations of $\Gamma_E(L)$ and $L_E(L)$ even for the largest separations allowed by the FOV [Fig. 6(a)]. Thus, we take L_E to be the average between the furthest maximum and minimum exhibited by $L_E(L)$, with alternative definitions not affecting the conclusions. In Figs. 6(b) and 6(c) we display L_E/L_f as a function of Re and Re_α. The ratio grows with increasing forcing: i.e., for the same geometric forcing scale, the correlation length scale increases with stronger forcing. This is consistent with the picture of the inverse energy cascade causing the merging of vortices into larger structures [4]. Meanwhile, Gallet and Young [40] demonstrated that the two-dimensional turbulence with an $n \times n$ array of alternating body forces results in the local vortex structure with typical size of $n^{-1} \times$ domain size, comparable to L_f in our system, at high Re. It implies that L_f will still remain an asymptote for the size of the vortex structure, which can account for a plateau reached at $L_E/L_f \approx 0.4$. It is similar to values reported in Faraday-wave-driven turbulence [8,41], and again the data collapse is much tighter when the data are plotted against Re_α.

A fundamental emergent behavior of 2D turbulence is the inverse energy cascade. This is characterized here by means of the third-order longitudinal structure function which can be written as $S_3^L(r) = \langle \delta u_L(r)^3 \rangle$, where $\delta u_L(r)$ is the longitudinal velocity difference between two points separated by a distance of r. In the case of 2D turbulence, $S_3^L(r) = \frac{1}{8}\zeta_\nu r^3$ in the range $L_\nu \ll r \ll L_f$ and $S_3^L(r) = \frac{3}{2}\epsilon_\alpha r$ in the range $L_f \ll r \ll L_\alpha$ are expected [42], where ζ_ν is the enstrophy dissipation rate by viscosity and ϵ_α is the energy dissipation rate due to large-scale drag, as illustrated in Fig. 7(a). A positive linear $S_3^L(r)$ in the range $L_f \ll r \ll L_\alpha$ was reported in Q2D flows of a soap film [43] and EML flows [44–47] as an indication of the inverse energy cascade.

Figure 7(b) shows the normalized third-order longitudinal structure function, $S_3^L(r)/u_{rms}^3$, for varying Reynolds numbers from SL2 configuration. It clearly demonstrates its transition to the

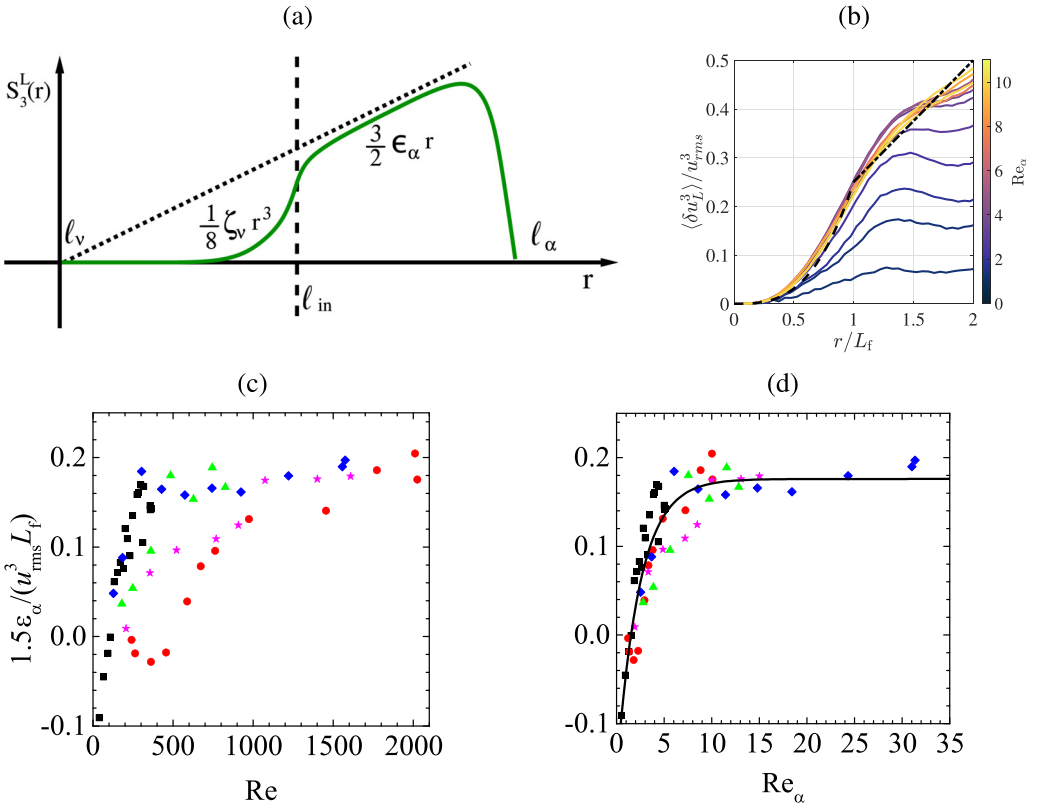

FIG. 7. (a) The third-order longitudinal structure function with two scaling ranges (adapted from [42] with permission). $\langle \delta u_L^3 \rangle \propto r^3$ in the smooth enstrophy cascade regime and $\propto r$ in the inverse energy cascade regime are expected for the 2D turbulence, where ζ_ν is the enstrophy dissipation rate by viscosity, ϵ_α is the energy dissipation rate due to large-scale drag, l_ν is the viscous length scale, l_{in} is the scale of forcing, and l_α is the length scale of frictional damping. (b) Normalized third-order longitudinal structure function ($\langle \delta u_L^3 \rangle / u_{rms}^3$) at varying Reynolds numbers from SL2 configuration. A black dashed line indicates the cubic trend, while a black dash-dotted line indicates the linear trend. The normalized large-scale frictional energy dissipation $[1.5\epsilon_\alpha/(u_{rms}^3/L_f)]$ is calculated by the slope in the range $r/L_f = [1.2\ 1.6]$, as a function of (c) Re and (d) Re_α. Again, a solid black curve indicates an exponential best fit. See Table II for explanation of the symbols.

positive linear $S_3^L(r)$ for sufficiently high Re. We estimate the normalized energy dissipation rate due to large-scale drag, $\frac{3}{2}\epsilon_\alpha/(u_{rms}^3 L_f)$ from the slope of $S_3^L(r)/u_{rms}^3$ in the range of $r/L_f = [1.2\ 1.6]$, and plot it as a function of Re and Re_α in Figs. 7(c) and 7(d). Again, it is clear that Re_α provides a closer data collapse than Re, and suggests a level above which the inverse energy cascade ensues.

A final hallmark feature of 2D turbulence we extract from the Eulerian fields is the absence of intermittency: both velocity fluctuations and velocity differences in the inertial range are expected to closely follow Gaussian distributions [48–50]. Figure 8(a) shows two probability density functions (PDFs) of $\boldsymbol{u}_{fluc}$ for two sample cases. The large-Re case approximates well a Gaussian distribution, while the small-Re case shows long exponential tails. The latter are the reflection of the regular vortex pattern (featuring marked minima and maxima of velocity at the core and periphery of vortices, respectively); this is distorted and ultimately destroyed with increasing forcing. Figures 8(b) and 8(c) show the kurtosis of PDF($\boldsymbol{u}_{fluc}$); Fig. 8(d) instead shows PDF[$\delta u_L(L_f)$], where $\delta u_L(L)$ is the longitudinal velocity difference at separation L, displaying an increasingly Gaussian behavior for L approaching and exceeding L_f. Figures 8(e) and 8(f) display the kurtosis of PDF[$\delta u_L(L_f)$],

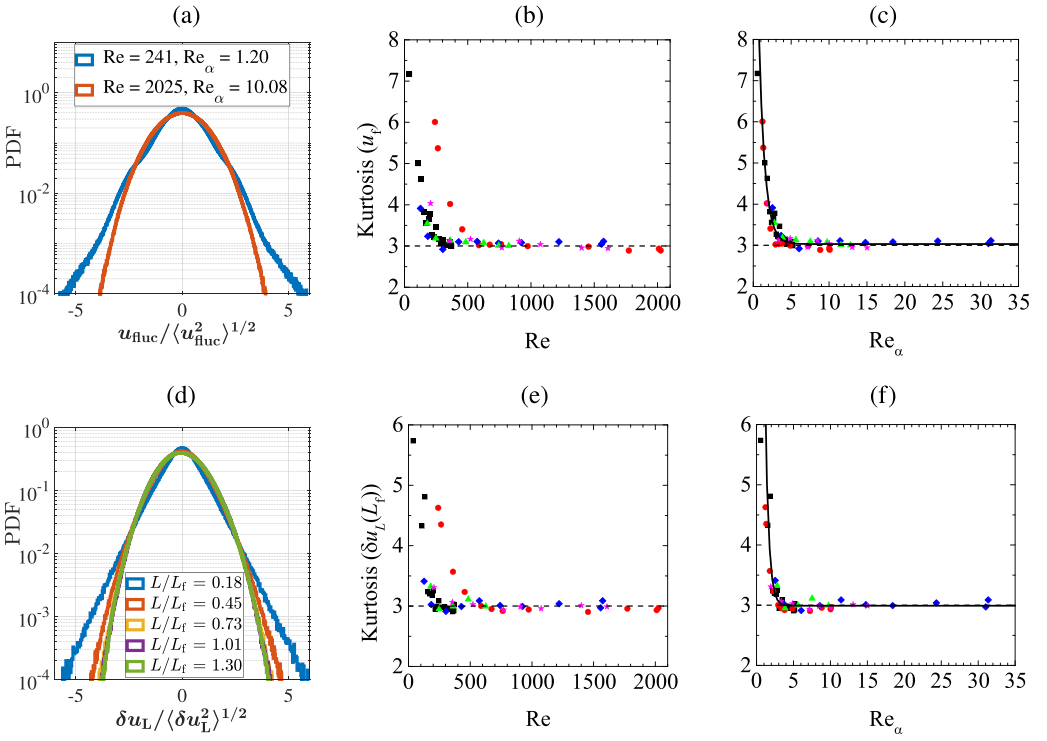

FIG. 8. (a) PDF of the fluctuation component of the Eulerian velocity. Re = 241, Re$_\alpha$ = 1.20 (blue) and Re = 2025, Re$_\alpha$ = 10.08 (red) cases are included for comparison. (b), (c) Kurtosis of the PDF as a function of (b) Re and (c) Re$_\alpha$. (d) An example of PDFs of the longitudinal velocity difference at different separations at Re = 2012, Re$_\alpha$ = 10.01. (e), (f) Kurtosis of the PDF as a function of (e) Re and (f) Re$_\alpha$. See Table II for explanation of the symbols.

with larger separations exhibiting analogous trends. The kurtosis of both classes of distributions is asymptotic to the Gaussian value of 3 with increasing forcing, again with Re$_\alpha$ capturing the universal trend much better than Re.

B. Lagrangian properties

The signatures of 2D turbulence can be recognized as well in Lagrangian quantities. Visual evidence of the emergence of turbulent behavior in tracer path lines is provided in Figs. 9(a)–9(c), which present 200 randomly selected trajectories at increasing Re for the SL2 configuration. For the same example cases, Fig. 9(d) illustrates the Lagrangian VACF between an initial time t_0 and a generic time t:

$$\Gamma_{\rm L}(t) = \frac{\langle \boldsymbol{u}_i(t_0)\cdot\boldsymbol{u}_i(t_0+t)\rangle_{i,t_0}}{\langle \boldsymbol{u}_i(t_0)\cdot\boldsymbol{u}_i(t_0)\rangle_{i,t_0}}, \tag{13}$$

where $\langle\cdot\rangle_i$ indicates ensemble averaging over all tracers i. The function oscillates regularly for relatively small Re, signaling the ordered and periodic behavior, while, for increasing forcing, it ultimately decays to negligible small values, as the tracers escape coherent vortices, move chaotically, and forget their previous state.

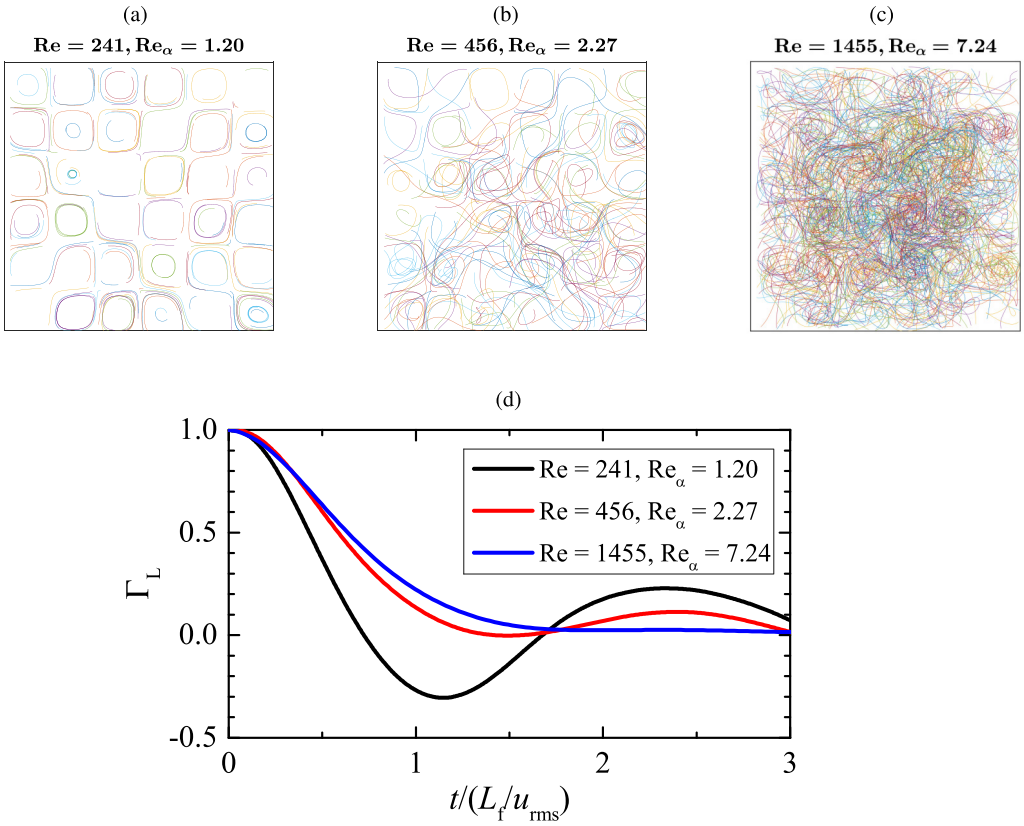

FIG. 9. Examples of Lagrangian trajectories. We draw 200 random trajectories with a minimum length of $2\omega_{\text{rms}}^{-1}$ in each case at (a) Re = 241, (b) Re = 456, and (c) Re = 1455. (d) Corresponding temporal Lagrangian VACFs are included accordingly.

To quantify the rate of Lagrangian dispersion, we consider the displacement r of the ith tracer from an initial position at time t_0, $r(t) = |\boldsymbol{x}_i(t_0 + t) - \boldsymbol{x}_i(t_0)|$. We then evaluate the turbulence diffusivity K from the slope of the mean-squared displacement (MSD):

$$\langle r^2(t)\rangle = \langle |\boldsymbol{x}_i(t_0 + t) - \boldsymbol{x}_i(t_0)|^2\rangle_{i,t_0}, \tag{14}$$

$$K = \frac{1}{2}\frac{d\langle r^2(t)\rangle}{dt}, \tag{15}$$

where the temporal derivative in (15) is calculated in the diffusive regime [26]. Figure 10(a) displays MSD as a function of time for various Re, illustrating the transition from the ballistic [$\langle r^2(t)\rangle \sim t^2$] to the diffusive regime [$\langle r^2(t)\rangle \sim t$]. Figures 10(b) and 10(c) show the normalized turbulence diffusivity plotted against both Re and Re$_\alpha$. The trend reflects the dramatic increase of the tracers' ability to disperse as the flow becomes chaotic and turbulent, before reaching a plateau at $K/(u_{\text{rms}}L_{\text{f}}) \approx 0.7$. Also for this Lagrangian observable, the friction Reynolds number is much more conducive to defining a general master curve, compared to its viscous counterpart. Again, the approximate value Re$_\alpha \approx 5$ appears as an appropriate level to predict the full development of the turbulent behavior, and the observable fully plateaus at Re$_\alpha \approx 10$.

Turbulent dispersion is also commonly characterized by pair statistics, typically via the square separation between the ith and jth particles, $[R(t) - R_0]^2 = [|\boldsymbol{x}_i(t_0 + t) - \boldsymbol{x}_j(t_0 + t)| - |\boldsymbol{x}_i(t_0) - \boldsymbol{x}_j(t_0)|]^2$, where R_0 is the initial separation at time t_0. Indeed, one of the first experimental

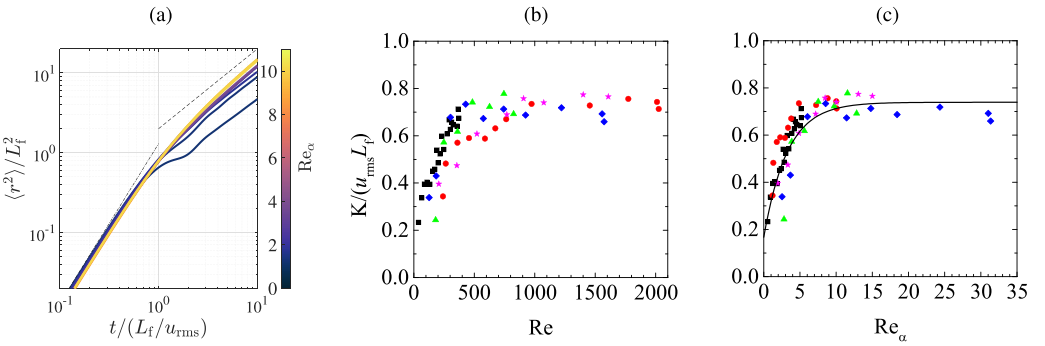

FIG. 10. Comparison of single particle dispersion rate under different flow conditions. (a) Normalized MSDs from SL2 configuration. A dash-dotted and dashed line indicate the initial ballistic scaling ($\sim t^2$) and the terminal diffusive scaling ($\sim t$) when $K/(u_{\mathrm{rms}}L_{\mathrm{f}}) = 1$, respectively. Dispersion rates of particles from different flow geometries are quantified by the normalized turbulent diffusivities, $K/(u_{\mathrm{rms}}L_{\mathrm{f}})$, and they are plotted as a function of (b) Re and (c) Re_α. A solid line indicates an exponentially asymptotic fitted line. See Table II for explanation of the symbols.

observations of the regime $[R(t) - R_0]^2 \sim t^3$ in the inertial range (famously predicted by Richardson [51]) was obtained in Q2D turbulence [52]. To facilitate the characterization of long pair trajectories over a broad range of separations, we advect imaginary tracers by interpolating the Eulerian velocity via a fourth-order Runge-Kutta scheme [22,53]. Moreover, to minimize cross-scale contamination that can affect finite-time statistics, rather than pair separations we consider the exit time t_{exit} required for a pair to reach a separation βR_0 [54]. We choose $\beta = 1.1$, and verify that the exact value of the constant does not influence the conclusions. This finite-space descriptor has reduced contributions from different dispersion regimes, since all considered particle pairs have narrowly distributed separations, $R_0 < R < \beta R_0$. In 2D turbulence the pair separation in the dissipative range ($R_0 \ll L_{\mathrm{f}}$) grows exponentially [54–56], leading to a constant t_{exit}, while it grows more rapidly in the inertial range ($R_0 > L_{\mathrm{f}}$), leading to $t_{\mathrm{exit}} \sim R_0^{2/3}$, as approximately verified by Rivera and Ecke [22].

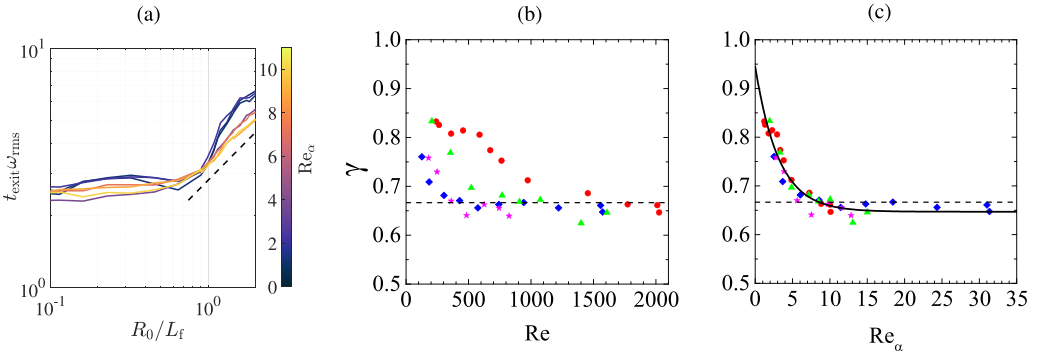

FIG. 11. (a) Normalized mean exit time ($t_{\mathrm{exit}}\omega_{\mathrm{rms}}$) at varying Reynolds numbers from SL2 configuration. A dashed line indicates a power-law exponent of 2/3 often expected for $R_0/L_{\mathrm{f}} > 1$ in turbulent flows. (b), (c) The scaling exponent of the exit time with the initial separation R_0, $t_{\mathrm{exit}} \sim R_0^{\gamma}$, calculated in the range $R_0/L_{\mathrm{f}} = [0.9\,2.0]$, as a function of (b) Re and (c) Re_α. A solid line is an exponential best fit. See Table II for explanation of the symbols.

Figure 11(a) displays t_{exit} as a function of initial separations for a range of Reynolds numbers in the SL2 configuration, with t_{exit} normalized by the root-mean-square vorticity, ω_{rms}. The exit time is approximately constant for $R_0 < L_{\text{f}}$, while for larger separations the trend grows steeper. In this range, for weak forcing t_{exit} is closer to a linear relation with the initial separation, which would correspond to a ballistic pair-separation scaling $[R(t) - R_0]^2 \sim t^2$; for stronger forcing the scaling $t_{\text{exit}} \sim R_0^{2/3}$ is approached for pair separations. This picture is confirmed in Figs. 11(b) and 11(c), where we plot the best-fit power-law exponent of t_{exit} in the range $0.9L_{\text{f}} < R_0 < 2.0L_{\text{f}}$ for different configurations. The range of R_0 is limited due to the difficulty of tracking pairs within the FOV at increasingly large separations and longer times, but it still allows us to discern clearly the trend: while pair dispersion is quasiballistic for the nonturbulent cases, the $t_{\text{exit}} \sim R_0^{2/3}$ regime (denoted by the dashed line) is approached with increasing Reynolds number. Once again, Re_α describes the behavior remarkably well across different configurations, with relatively small changes beyond $\text{Re}_\alpha \approx 5$.

IV. DISCUSSION

The previous section has confirmed that Re_α has a primary role in determining the emergence and development of turbulent fluctuations in EML Q2D. This is consistent with the notion that hallmark turbulent processes, such as the growth of the fluctuating energy, the energy cascade, and turbulent dispersion, acquire their self-similar character over the inertial range $L_{\text{f}} \ll L \ll L_\alpha$, whose extent is quantified by Re_α. Two clarifications are in order. First, the present analysis does not address the hydrodynamic instabilities that lead to periodic, nonperiodic, or chaotic motion [57], but rather considers observables commonly used to identify and characterize turbulent flows. Therefore, we make no claim on whether Re or Re_α is the most appropriate parameter for the characterization of those instabilities. Second, we have focused on essential but specific aspects of 2D turbulence, in particular those primarily associated to the energetic scales. If one focuses on small-scale processes such as vorticity gradient stretching, which takes place over the enstrophy cascade range, $L_\nu \ll L \ll L_{\text{f}}$ [58,59], the conclusions may change.

We have presented and compared results from separate experiments, in each of which (local) Re and Re_α are always positively correlated. To further corroborate our findings, we apply a simple modification to the EML system which causes Re and Re_α to vary spatially in opposite directions: we create a wedge-shaped double-layer configuration with varying depth by placing a spacer under one side of the flow tray as illustrated in Fig. 12(a). The bottom lubrication layer has linearly increasing thickness along the x direction from 2 to 8 mm, while the top conductive layer thickness remains constant at 2 mm. On the one hand, considering mass balance across the yz plane, $u_x(x)A_{yz}(x) = u_x(x)[Hh(x)] = \text{const}$, one can expect $u_x(x)$ to be inversely proportional to $h(x)$ which is linearly increasing with x. Consequently, Re is greater at the thinner layer (smaller x) and smaller at the thicker layer (greater x). On the other hand, $\text{Re}_\alpha \propto u_{\text{rms}}/\alpha \propto u_{\text{rms}}h^2$, so Re_α is expected to decrease with increasing x. Figure 12(b) shows that Re and Re_α exhibit the exactly opposite behaviors over x as intended, and Fig. 12(c) evidently indicates that turbulent flow appears in the high Re_α or low Re zone rather than the high Re or low Re_α zone. Figures 12(c) and 12(d) map joint PDFs of the local turbulent intensity versus Re and Re_α in each grid position, respectively. While the local turbulence intensity is correlated with Re either weakly or even negatively, it appears positively correlated with local Re_α. Moreover, the joint PDF peaks in Fig. 12(d) agree well with the asymptotic relation (black dashed) that we already observed in Fig. 5(b), which undoubtedly proves that Re_α rather than Re should play a key role in emergence of the EML Q2D turbulent flows.

The primary role of Re_α over Re is also consistent with the fact that, in Q2D flows moving over a boundary, the bottom friction (expressed over the entire domain footprint) naturally dominates over viscous dissipation (expressed mostly in the high-strain filaments within the fluid layer). From the very definition of Re and Re_α, the ratio of Rayleigh friction forces over viscous forces scales as $\text{Re}/\text{Re}_\alpha$, which for a single-layer setup is approximately $(\pi^2/2)(L_{\text{f}}/h)^2$. The requirement of a relatively thin layer to reach the Q2D condition (e.g., $L_{\text{f}}/h > 3$ in our experiments) implies that this

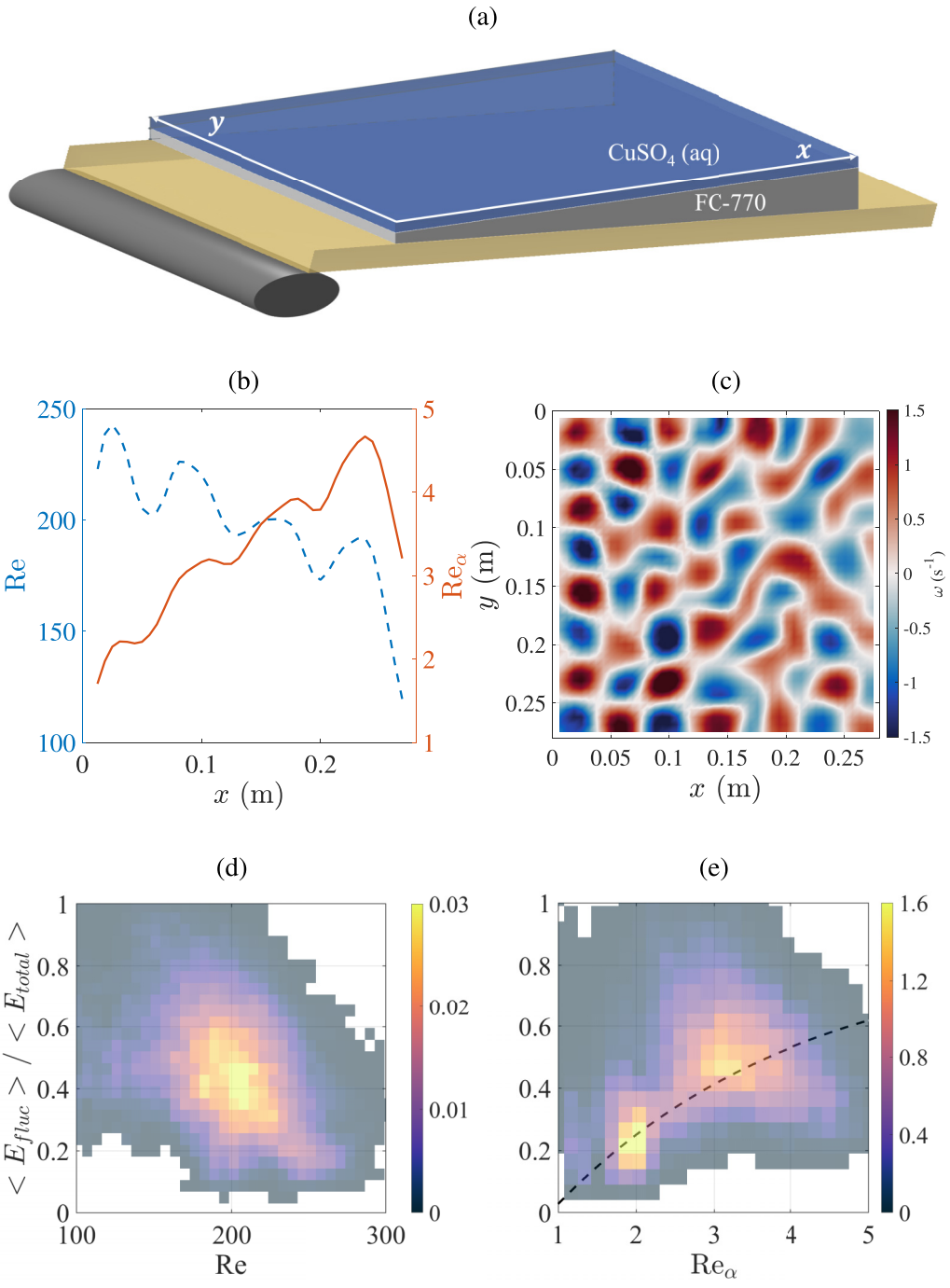

FIG. 12. Results from a tilted tray experiment. (a) By placing a spacer under the tray, the bottom layer (FC-770) thickness increases linearly over x from 2 to 8 mm, while the top layer [$CuSO_4(aq)$] thickness is maintained at 2 mm. Note that it is not drawn to scale but exaggerates the fluid depth variations as a visual aid. (b) y-averaged Re (blue dashed) and Re_α (red) as a function of x position. (c) A snapshot of Eulerian velocity and vorticity maps. (d), (e) A joint PDF of turbulence intensity vs (d) Re and (e) Re_α. A black dashed line is the exponential best fit taken from Fig. 5(b).

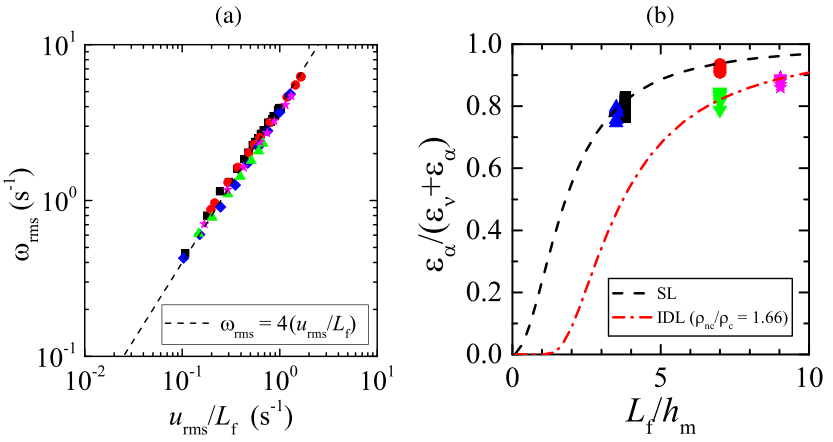

FIG. 13. (a) The root-mean-squared vorticity vs the root-mean-squared velocity. A dashed line indicates $\omega_{\rm rms} = 4u_{\rm rms}/L_{\rm f}$. (b) The fraction of energy dissipation by friction as a function of an effective aspect ratio $(L_{\rm f}/h_{\rm m})$, where $h_{\rm m} = h$ for a single-layer and $(h_{\rm c}h_{\rm NC})^{1/2}$ for a double-layer setup. The lines represent predictions based on $\omega_{\rm rms} = 4u_{\rm rms}/L_{\rm f}$. The black dashed line represents a single-layer configuration, while the red dash-dotted line corresponds to an immiscible double-layer configuration with a density ratio of 1.66, which matches our choice of fluids. See Table II for explanation of the symbols.

ratio be at least $O(10)$, which is indeed the case in the current paper where the ratio lies between 60 and 240. Similar considerations apply to double-layer setups for practically usable pairs of fluids. The above indicates that input forcing and friction damping will dominate over viscous dissipation in the energy balance. The quantitative fraction of the energy transfer rate associated with each dissipative process is not known *a priori*. However, the 2D turbulence scaling $\epsilon_\nu \approx \nu\omega_{\rm rms}^2$, $\epsilon_\alpha \approx \alpha u_{\rm rms}^2$, and $\omega_{\rm rms} \sim u_{\rm rms}/L_{\rm f}$ [6,26] suggest that such fraction may be reliably estimated. Here we posit that the flow in the Q2D EML system can be described, in first approximation, as an ensemble of solid-body vortices of diameter $L_{\rm f}$ and tangential velocity $u_{\rm rms}$ along the perimeter. The vorticity associated to each vortex is then $\omega = 4u_{\rm rms}/L_{\rm f}$. Figure 13(a), plotting $\omega_{\rm rms}$ versus $u_{\rm rms}/L_{\rm f}$ for all the considered cases, demonstrates that not only the scaling but also the geometric prefactor hold remarkably well across the entire range of our data sets, and (perhaps surprisingly) even for the fully turbulent cases. This leads to

$$\frac{\epsilon_\alpha}{\epsilon_\nu} \approx \frac{\alpha u_{\rm rms}^2}{\nu\omega_{\rm rms}^2} \approx \frac{\alpha L^2}{16\nu} \tag{16}$$

or, for a single-layer configuration,

$$\frac{\epsilon_\alpha}{\epsilon_\nu} \approx \frac{\pi^2}{32}\left(\frac{L_{\rm f}}{h}\right)^2, \tag{17}$$

and for a double-layer configuration, introducing $h_{\rm m} = (h_{\rm c}h_{\rm NC})^{1/2}$,

$$\frac{\epsilon_\alpha}{\epsilon_\nu} \approx \frac{1}{16}\left(\frac{\rho_{\rm NC}}{\rho_{\rm c}}\right)\left(\frac{L_{\rm f}}{h_{\rm m}}\right)^2. \tag{18}$$

These relations suggest that the fraction of energy dissipation by friction depends on an (effective) aspect ratio of the Q2D geometry. With the quantitative estimate of the prefactor we see that, if we take for example $L_{\rm f}/h \approx 3$ as the minimum requirement for a single-layer Q2D geometry, such a ratio $\approx$2.78 at least. Thus, the fraction of energy input dissipated by viscosity, $\epsilon_\nu/(\epsilon_\nu + \epsilon_\alpha)$, is only about 1/4 at most. Again, similar considerations apply to double-layer systems. We stress that this quantitative estimate is made possible by the quantitative agreement in Fig. 13(a), which

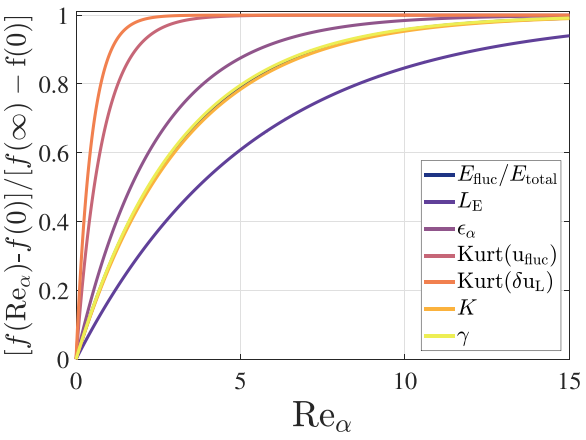

FIG. 14. Normalized exponential fitting functions vs Re_α. See Appendix C for each function.

demonstrates the validity of the prefactor 4 in the vorticity scaling. The relation can be inverted, to determine the aspect ratio needed to reach a prescribed fraction of frictional dissipation as shown in Fig. 13(b).

Based on the results above, Fig. 14 summarizes asymptotic behaviors of the tested variables as Re_α increases. The chosen exponential fit is of the type $a + b\exp(-\mathrm{Re}_\alpha/c)$, where c naturally characterizes the exponential approach to the asymptote. Note that $c \approx 5$ for the slowest converging quantity (L_{E}). Here, each exponential best-fit function listed in Appendix C is further normalized such that it starts from zero at $\mathrm{Re}_\alpha = 0$ and asymptotically approaches 1 as $\mathrm{Re}_\alpha \to \infty$, for fair comparison among different observables. Other forms of the trend line, such as power laws, do not provide equally good fit to the data, as shown in Appendix D. At $\mathrm{Re}_\alpha \approx 5$, all attain over 80% of the plateau value except for L_{E} which achieves about 60% of the asymptotic limit. The slower evolution of L_{E} could be attributed to the local vortex structures with typical size of L_{f} surviving even at high flow rate limit [40]. At $\mathrm{Re}_\alpha \approx 10$, more than 95% of the limit is attained by six of seven observables, while even the slowest evolving L_{E} reaches 85% of the plateau. Based on the trend, for the considered class of flows, at least $\mathrm{Re} \approx 5$ is found to be a necessary condition for the full development of two-dimensional turbulence, though the asymptotic behavior is approached only above $\mathrm{Re} \approx 10$. We remark that these do not constitute critical thresholds, as the observables are found to smoothly and exponentially approach the asymptotic values.

V. CONCLUSIONS

We have used two setups and five Q2D EML configurations to experimentally investigate the emergence and development of 2D turbulence in 58 different experiments, over a wide range of Re and Re_α. The main conclusions of this paper can be summarized as follows.

(1) All considered turbulence quantities (Eulerian and Lagrangian, single-point and two-point statistics) collapse on master curves against Re_α spanning over two decades and across different flow configurations (single-layer, miscible and immiscible double-layer).

(2) The friction coefficient α can be estimated with reasonable accuracy via a simple linear shear assumption, allowing us to readily evaluate Re_α. On the other hand, for the type of systems we considered (the most common in laboratory studies of 2D turbulence) even $\mathrm{Re} = 1000$ may not be sufficient to reach fully developed turbulence. In fact, there is no direct connection between Re and the growth of the turbulent kinetic energy in this class of flows, as shown by dedicated experiments that decouple both Reynolds numbers. Therefore, in studies focused on the inverse energy cascade subrange, it is crucial to measure (or estimate) and report Re_α.

(3) Not all quantities approach the fully developed or asymptotic state of turbulence equally fast, the kurtosis being the fastest to approach a Gaussian behavior, with the Eulerian integral scale being the slowest to reach an asymptotic state. This indicates that multiple observables should be considered to establish whether the fully developed turbulence state has been reached.

(4) The approach to the asymptotic values of the various quantities is well described by an exponential curve, which does not suggest a sharp transition over a critical threshold. Based on the observations, we propose $\mathrm{Re}_\alpha \approx 5$ as a necessary condition for fully developed turbulence in this class of laboratory flows, while the asymptotic state is approximately reached for $\mathrm{Re}_\alpha \approx 10$. Further studies are warranted to clarify whether such levels can be applied to other laboratory Q2D flow or to computational setups.

(5) For the considered EML systems, the scaling of the rms vorticity indicates that the velocity field can be rationalized as a superposition of solid-body vortices of diameter L_f and azimuthal velocity u_rms. This leads to a simple expression for the fraction of the energy input transported to the larger scales. This fraction is at least $3/4$ for typical EML systems in which $L_\mathrm{f}/h > 3$.

We remark that the condition $\mathrm{Re}_\alpha \approx L_\alpha/L_\mathrm{f} \approx 5$ still warrants only a limited scale separation, which is likely to inhibit the inverse energy cascade [59]. Indeed our results do indicate that larger values do produce some evolution of the observables in the range $\mathrm{Re}_\alpha \approx 5$–10. However, those changes are marginal compared to the dramatic transformations undergone by the flow in the range $\mathrm{Re}_\alpha \approx 0.5$–5.

The importance of Re_α in determining the emergence and development of the turbulence does not imply Re has a negligible role in defining the flow properties. On one side, Re sets the extent of the enstrophy cascade subrange. On the other hand, the fraction of the energy input transported to the larger versus the smaller scales is set by the ratio $\mathrm{Re}_\alpha/\mathrm{Re}$. Therefore, the full definition of the system requires specifying both parameters. In fact, some of the scatter when plotting the observables versus Re_α may depend on Re effects which are not accounted for by the simple functional dependence.

While the present conclusions are based on Q2D flow in EML systems, their applicability to other 2D turbulence setups is supported by the different configurations investigated, the wide range of Eulerian and Lagrangian observables considered, and the generality of the physical arguments. Further studies, however, are warranted to extend these quantitative findings to other realizations of 2D turbulence. Moreover, while we have only considered observables associated to the velocity field, it will be important to verify whether the proposed level for Re_α also applies to turbulent scalar fluxes, which also obey inertial-range scaling [60].

APPENDIX A

In all experiments, both PIV and PTV analyses were conducted using the same image sequence. The Eulerian observables obtained from each analysis exhibit strong quantitative agreement. As an illustrative example, we present the Eulerian VACF in Fig. 15. Notably, the results are nearly identical, with the only distinction being that the PIV-derived data possess a lower spatial resolution due to the limitations imposed by the PIV grid size.

APPENDIX B

We conducted a spin-down experiment to estimate the friction coefficient by observing the decay of mean kinetic energy (Fig. 3). Prior to discontinuing the forcing, we ensured that the flow had attained a steady state, enabling us to calculate the turbulence intensity for each case. Figure 16 presents the turbulence intensity as a function of Re_α determined from the spin-down experiment. Notably, the exponential best fit obtained from Fig. 5(b) based on the theoretically derived Re_α still accurately depicts the transition even when using the measured Re_α. Therefore, we believe that our utilization of Re_α based on a rather simplistic linear friction damping is well founded.

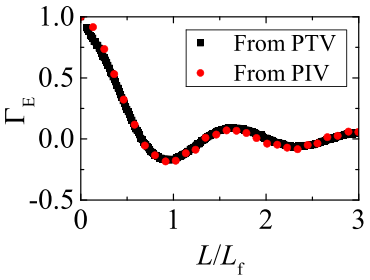

FIG. 15. Comparison of the Eulerian VACF derived from PTV and PIV analyses applied to the same image sequence acquired from the SL2 configuration at Re = 673. The Eulerian VACF demonstrates nearly identical behavior irrespective of whether it is obtained from PTV or PIV.

APPENDIX C

We provide exponential best-fit functions imposed on data plotted against Re_α, in Figs. 5(b), 6(c), 7(d), 8(c), 8(f), 10(c), and 11(c), respectively:

$$\langle E_{\mathrm{fluc}}\rangle/\langle E_{\mathrm{total}}\rangle = 0.853 - 1.13\exp(-\mathrm{Re}_\alpha/3.18), \tag{C1}$$

$$L_{\mathrm{E}}/L_{\mathrm{f}} = 0.407 - 0.219\exp(-\mathrm{Re}_\alpha/5.33), \tag{C2}$$

$$\tfrac{3}{2}\epsilon_\alpha/\left(u_{\mathrm{rms}}^3/L_f\right) = 0.176 - 0.331\exp(-\mathrm{Re}_\alpha/2.40), \tag{C3}$$

$$\mathrm{Kurt}[u_{\mathrm{f}}] = 3.03 + 13.0\exp(-\mathrm{Re}_\alpha/0.791), \tag{C4}$$

$$\mathrm{Kurt}[\delta u_{\mathrm{L}}(L_{\mathrm{f}})] = 2.99 + 41.3\exp(-\mathrm{Re}_\alpha/0.468), \tag{C5}$$

$$K/(u_{\mathrm{rms}}L_{\mathrm{f}}) = 0.793 - 0.572\exp(-\mathrm{Re}_\alpha/3.26), \tag{C6}$$

$$\gamma = 0.647 + 0.298\exp(-\mathrm{Re}_\alpha/3.14). \tag{C7}$$

We have proposed exponential fitting functions to describe the asymptotic transitions of the tested observables and the development of 2D turbulence, which are provided in Appendix C. We attempted various forms of trend line fits, including power laws of the form $a + b|\mathrm{Re}_\alpha - c|^n$, where c represents a critical onset of development. However, these fits appeared to be inferior to the best exponential fits we present as seen in Fig. 17.

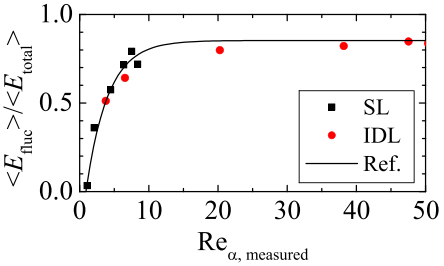

FIG. 16. The steady-state turbulence intensity prior to each spin-down experimental condition as a function of the measured Re_α. Each data point was obtained at the steady state prior to the spin-down experiment corresponding to Fig. 3(b). A black solid line taken from Fig. 5(b) is added for comparison.

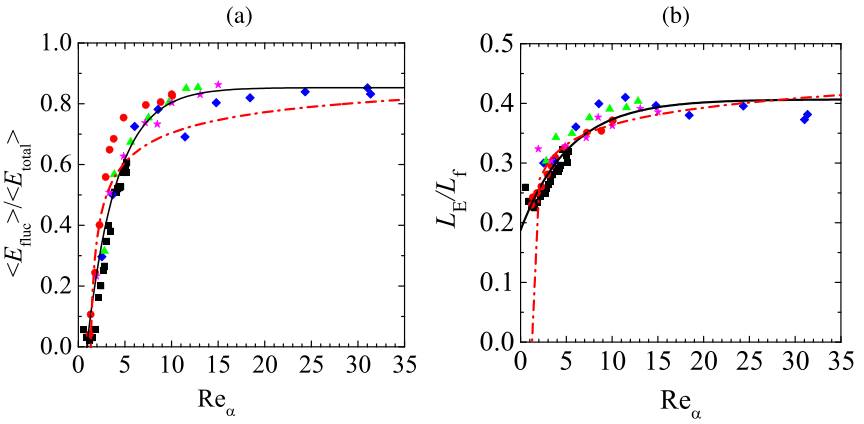

FIG. 17. Comparison between the best exponential fit (black solid line) and a power-law fit (red dash-dotted line) for (a) the turbulence intensity and (b) the Eulerian integral scale. The exponential fit is provided in Appendix C. The power-law fit follows the form $a + b|\mathrm{Re}_\alpha - c|^n$. See Table II for explanation of the symbols.

[1] G. J. F. van Heijst and H. J. H. Clerex, Laboratory modeling of geophysical vortices, Annu. Rev. Fluid Mech. **41**, 143 (2009).

[2] A. Pouquet and R. Marino, Geophysical Turbulence and the Duality of the Energy Flow Across Scales, Phys. Rev. Lett. **111**, 234501 (2013).

[3] G. K. Vallis, *Atmospheric and Oceanic Fluid Dynamics* (Cambridge University, New York, 2017).

[4] P. Tabeling, Two-dimensional turbulence: A physicist approach, Phys. Rep. **362**, 1 (2002).

[5] H. J. H. Clercx and G. J. F. van Heijst, Two-dimensional Navier-Stokes turbulence in bounded domains, Appl. Mech. Rev. **62**, 020802 (2009).

[6] G. Boffetta and R. E. Ecke, Two-dimensional turbulence, Annu. Rev. Fluid Mech. **44**, 427 (2012).

[7] H. Kellay and W. I. Goldburg, Two-dimensional turbulence: A review of some recent experiments, Rep. Prog. Phys. **65**, 845 (2002).

[8] A. von Kameke, F. Huhn, G. Fernández-García, A. P. Muñuzuri, and V. Pérez-Muñuzuri, Double Cascade Turbulence and Richardson Dispersion in a Horizontal Fluid Flow Induced by Faraday Waves, Phys. Rev. Lett. **107**, 074502 (2011).

[9] N. Francois, H. Xia, H. Punzmann, and M. Shats, Inverse Energy Cascade and Emergence of Large Coherent Vortices in Turbulence Driven by Faraday Waves, Phys. Rev. Lett. **110**, 194501 (2013).

[10] R. A. D. Akkermans, A. R. Cieslik, L. P. J. Kamp, R. R. Trieling, H. J. H. Clercx, and G. J. F. van Heijst, The three-dimensional structure of an electromagnetically generated dipolar vortex in a shallow fluid layer, Phys. Fluids **20**, 116601 (2008).

[11] J. Tithof, B. C. Martell, and D. H. Kelley, Three-dimensionality of one-and two-layer electromagnetically driven thin-layer flows, Phys. Rev. Fluids **3**, 064602 (2018).

[12] S. Discetti and F. Coletti, Volumetric velocimetry for fluid flows, Meas. Sci. Technol. **29**, 042001 (2018).

[13] B. C. Martell, J. Tithof, and D. H. Kelley, Comparing free surface and interface motion in electromagnetically driven thin-layer flows, Phys. Rev. Fluids **4**, 043904 (2019).

[14] R. H. Kraichnan and D. Montgomery, Two-dimensional turbulence, Rep. Prog. Phys. **43**, 547 (1980).

[15] H. J. H. Clercx and G. J. F. van Heijst, Dissipation of coherent structures in confined two-dimensional turbulence, Phys. Fluids **29**, 111103 (2017).

[16] T. Wu and W. J. T. Bos, Cascades of enstrophy and helicity in turbulence without vortex stretching, Phys. Rev. Fluids **7**, 094601 (2022).

[17] W. J. Bos and J. P. Bertoglio, Large-scale bottleneck effect in two-dimensional turbulence, J. Turbul. **10**, N30 (2009).
[18] P. Tabeling, S. Burkhart, O. Cardoso, and H. Willaime, Experimental Study of Freely Decaying Two-Dimensional Turbulence, Phys. Rev. Lett. **67**, 3772 (1991).
[19] J. Paret and P. Tabeling, Experimental Observation of the Two-Dimensional Inverse Energy Cascade, Phys. Rev. Lett. **79**, 4162 (1997).
[20] B. S. Williams, D. Marteau, and J. P. Gollub, Mixing of a passive scalar in magnetically forced two-dimensional turbulence, Phys. Fluids **9**, 2061 (1997).
[21] H. J. H. Clercx, G. J. F. van Heijst, and M. L. Zoeteweij, Quasi-two-dimensional turbulence in shallow fluid layers: The role of bottom friction and fluid layer depth, Phys. Rev. E **67**, 066303 (2003).
[22] M. K. Rivera and R. E. Ecke, Pair Dispersion and Doubling Time Statistics in Two-Dimensional Turbulence, Phys. Rev. Lett. **95**, 194503 (2005).
[23] R. Ni, G. A. Voth, and N. T. Ouellette, Extracting turbulent spectral transfer from under-resolved velocity fields, Phys. Fluids **26**, 105107 (2014).
[24] M. K. Rivera and R. E. Ecke, Lagrangian statistics in weakly forced two-dimensional turbulence, Chaos **26**, 013103 (2016).
[25] L. Fang and N. T. Ouellette, Multiple stages of decay in two-dimensional turbulence, Phys. Fluids **29**, 111105 (2017).
[26] P. A. Davidson, *Turbulence: An Introduction for Scientists and Engineers* (Oxford University, New York, 2015).
[27] P. Manneville, Spatiotemporal intermittency, in *Nonlinear Evolution of Spatio-Temporal Structures in Dissipative Continuous Systems* (Springer, New York, 1990), pp. 545–552.
[28] D. Rothstein, E. Henry, and J. P. Gollub, Persistent patterns in transient chaotic fluid mixing, Nature (London) **401**, 770 (1999).
[29] G. A. Voth, T. C. Saint, G. Dobler, and J. P. Gollub, Mixing rates and symmetry breaking in two-dimensional chaotic flow, Phys. Fluids **15**, 2560 (2003).
[30] N. T. Ouellette, P. J. J. O'Malley, and J. P. Gollub, Transport of Finite-Sized Particles in Chaotic Flow, Phys. Rev. Lett. **101**, 174504 (2008).
[31] H. Xia, N. Francois, H. Punzmann, and M. Shats, Taylor Particle Dispersion during Transition to Fully Developed Two-Dimensional Turbulence, Phys. Rev. Lett. **112**, 104501 (2014).
[32] J. Sommeria, Experimental study of the two-dimensional inverse energy cascade in a square box, J. Fluid Mech. **170**, 139 (1986).
[33] G. Michel, J. Herault, F. Pétrélis, and S. Fauve, Bifurcations of a large-scale circulation in a quasi-bidimensional turbulent flow, Europhys. Lett. **115**, 64004 (2016).
[34] E. Stamhuis and W. Thielicke, PIVlab—towards user-friendly, affordable and accurate digital particle image velocimetry in MATLAB, J. Open Source Softw. **2**, e30 (2014).
[35] J. C. Crocker and D. G. Grier, Methods of digital video microscopy for colloidal studies, J. Colloid Interface Sci. **179**, 298 (1996).
[36] N. F. Bondarenko, M. Z. Gak, and F. V. Dolzhanskii, Laboratory and theoretical models of plane periodic flow, Akademiia Nauk SSSR Fizika Atmosfery i Okeana **15**, 1017 (1979).
[37] D. H. Kelley and N. T. Ouellette, Using particle tracking to measure flow instabilities in an undergraduate laboratory experiment, Am. J. Phys. **79**, 267 (2011).
[38] D. Lucas and R. R. Kerswell, Recurrent flow analysis in spatiotemporally chaotic 2-dimensional Kolmogorov flow, Phys. Fluids **27**, 045106 (2015).
[39] Y. Liao, D. H. Kelley, and N. T. Ouellette, Effects of forcing geometry on two-dimensional weak turbulence, Phys. Rev. E **86**, 036306 (2012).
[40] B. Gallet and W. R. Young, A two-dimensional vortex condensate at high Reynolds number, J. Fluid Mech. **715**, 359 (2013).
[41] H. Xia, N. Francois, H. Punzmann, and M. Shats, Lagrangian scale of particle dispersion in turbulence, Nat. Commun. **4**, 2013 (2013).
[42] A. Alexakis and L. Biferale, Cascades and transitions in turbulent flows, Phys. Rep. **767-769**, 1 (2018).

[43] A. Belmonte, W. I. Goldburg, H. Kellay, M. A. Rutgers, B. Martin, and X. L. Wu, Velocity fluctuations in a turbulent soap film: The third moment in two dimensions, Phys. Fluids **11**, 1196 (1999).
[44] M. G. Shats, H. Xia, H. Punzmann, and G. Falkovich, Suppression of Turbulence by Self-Generated and Imposed Mean Flows, Phys. Rev. Lett. **99**, 164502 (2007).
[45] H. Xia, H. Punzmann, G. Falkovich, and M. G. Shats, Turbulence-Condensate Interaction in Two Dimensions, Phys. Rev. Lett. **101**, 194504 (2008).
[46] H. Xia, M. Shats, and G. Falkovich, Spectrally condensed turbulence in thin layers, Phys. Fluids **21**, 125101 (2009).
[47] H. Xia, D. Byrne, G. Falkovich, and M. Shats, Upscale energy transfer in thick turbulent fluid layers, Nat. Phys. **7**, 321 (2011).
[48] L. M. Smith and V. Yakhot, Bose Condensation and Small-Scale Structure Generation in a Random Force Driven 2D Turbulence, Phys. Rev. Lett. **71**, 352 (1993).
[49] J. Paret and P. Tabeling, Intermittency in the two-dimensional inverse cascade of energy: Experimental observations, Phys. Fluids **10**, 3126 (1998).
[50] G. Boffetta, A. Celani, and M. Vergassola, Inverse energy cascade in two-dimensional turbulence: Deviations from Gaussian behavior, Phys. Rev. E **61**, R29 (2000).
[51] L. F. Richardson, Atmospheric diffusion shown on a distance-neighbour graph, Proc. R. Soc. A **110**, 709 (1926).
[52] M. Jullien, J. Paret, and P. Tabeling, Richardson Pair Dispersion in Two-Dimensional Turbulence, Phys. Rev. Lett. **82**, 2872 (1999).
[53] H. Xia, N. Francois, H. Punzmann, and M. Shats, Tunable diffusion in wave-driven two-dimensional turbulence, J. Fluid Mech. **865**, 811 (2019).
[54] J. P. L. C. Salazar and L. R. Collins, Two-particle dispersion in isotropic turbulent flows, Annu. Rev. Fluid Mech. **41**, 405 (2009).
[55] R. Dhariwal and A. D. Bragg, Fluid particles only separate exponentially in the dissipation range of turbulence after extremely long times, Phys. Rev. Fluids **3**, 034604 (2018).
[56] R. Dhariwal and A. D. Bragg, Small-scale dynamics of settling, bidisperse particles in turbulence, J. Fluid Mech. **839**, 594 (2018).
[57] J. Tithof, B. Suri, R. K. Pallantla, R. O. Grigoriev, and M. F. Schatz, Bifurcations in a quasi-two-dimensional kolmogorov-like flow, J. Fluid Mech. **828**, 837 (2017).
[58] S. Chen, R. E. Ecke, G. L. Eyink, X. Wang, and Z. Xiao, Physical Mechanism of the Two-Dimensional Enstrophy Cascade, Phys. Rev. Lett. **91**, 214501 (2003).
[59] Z. Zhou, L. Fang, N. T. Ouellette, and H. Xu, Vorticity gradient stretching in the direct enstrophy transfer process of two-dimensional turbulence, Phys. Rev. Fluids **5**, 054602 (2020).
[60] W. J. T. Bos, B. Kadoch, K. Schneider, and J.-P. Bertoglio, Inertial range scaling of the scalar flux spectrum in two-dimensional turbulence, Phys. Fluids **21**, 115105 (2009).